A standardized Physical Equivalent Temperature urban heat map at 1-m spatial resolution to facilitate climate stress tests in the Netherlands

S. Koopmans [*], B.G. Heusinkveld, G.J. Steeneveld

Wageningen University and Research, Meteorology and Air Quality Section, Wageningen, the Netherlands

A B S T R A C T

In the Netherlands, municipalities and other sub-national governments have to conduct climate stress tests to examine the societal impact of heat load by citizens. So far, these parties have been hindered by the abundance of contrasting urban heat maps produced with different metrics and methods by different agencies. To unify the stress tests, we present a methodology for a standardized urban heat map at 1-m spatial resolution by selecting the Physical Equivalent Temperature (PET) as metric for heat stress.

First we present an empirical regression model for PET, based on a variety of weather data and street configurations in the human thermal energy balance model Rayman. Thereafter, this empirical PET-model is evaluated for the midsized town Wageningen (the Netherlands). Meteorological observations taken at a nearby reference site and straightforward geographical data have been used as model input. Also, established methods were applied and elaborated to account for the urban heat island effect and wind speed reduction in the city. The presented method is validated against bike traverse observations of PET. Wind speed is the most challenging feature to map, due to its unsteady and local behaviour in cities.

As a result, an afternoon averaged PET heat map is demonstrated as standard for an extreme heat day (1:1000 summer half year days), and a cumulative exceedance PET heat map for a representative year. Furthermore, a heat map is projected for 2050 according a warm climate change scenario.

1. Introduction

Climate change and the urbanization urges authorities to investigate whether climate adaptation measures should be taken [1], via so called climate stress tests in the Netherlands. A climate stress test assesses bottlenecks and vulnerabilities in the physical and socio-economic infrastructure in case of flooding, drought and ultimately also heat stress. This study focuses on heat stress, and develops high-resolution (1 m) heat maps that indicate the hot spots and help decision makers to plan their climate adaptation and infrastructural measures. So far many different urban heat maps circulate right now indicating different heat metrics, which may confuse stakeholders of municipalities and subnational governments. These metrics may vary from remote sensing based surface temperatures [2], urban heat islands (UHI) based on air temperature [3], to the number of tropical nights (nights with minimum temperatures above 20 °C) [4]. To unify the heat maps the Dutch Ministry of Infrastructure asked a broad consortium to select one heat metric, and to develop a recipe to create an accompanying heat map.

Heat waves are projected to become more severe and have longer durations in Europe [5]. The higher temperatures more often lead to thermal discomfort and heat stress with adverse effects on human health and labour productivity [6]. Under high-risk groups like elderly and people with cardiovascular diseases, higher mortality rates have been observed in recent severe heat waves in Europe in 2003 and 2006 [7,8] and the number of heat related deaths are projected to increase in the climate scenarios [9,10]. Most people suffer from heat stress in cities, which also result in higher mortality rates [11–13]. This is related to higher air temperatures relative to their rural counterparts which is known as the UHI. Higher temperatures are induced by the urban morphological characteristics [14] and reduced evaporation by impervious surfaces [15]. Due to the relatively high heat capacity of the urban fabric, higher temperatures are especially observed in evenings and early nights.

Air temperatures, however, do explain only a small part how humans experience heat. More important is to include factors which affect the heat release of the human body. These factors include the wind speed,

which provides ventilation and ameliorates heat stress, humidity which determines how efficient humans can release heat by transpiration and radiation load, which has the largest contribution from solar radiation. One of the thermal comfort indexes accounting for these factors is the Physiological Equivalent Temperature (PET) [16]. PET classes have previously been constructed to define different grades of thermal perception [17]. In case of low wind speed and low insolation due to cloudiness, the air temperature is close to the PET. In sunlit calm conditions during summer the PET can exceed the air temperature by 20 °C.

Compared to an open rural environment, the urban PET increase is expected to exceed the air temperature increase [18,19], due to relatively low wind speeds induced by a high surface roughness and multiple reflections of solar radiation from buildings. Wind speed and incoming radiation vary on a very small scale in cities. Therefore, heat maps are calculated at a 1-m resolution to reveal small-scale hotspots to offer decision makers insight in the vulnerable locations in their urban environment, and are an indispensable tool needed for climate stress tests.

A novelty of the presented heat maps is the combination of different state-of-the-art empirical meteorological models and GIS-based tools at 1-m resolution, which is subsequently tested against in situ observations in the urban environment. Applying empirical models avoids expensive high-resolution numerical simulations, but it allows for relatively easy to implement routines. For instance, urban air temperatures and wind speed can be estimated with routine weather observations and information about land use and geometries of buildings and trees [20,21]. Heat maps are demonstrated for the town of Wageningen in the Netherlands for a representative hot day afternoon and an average summer half year (April–September). In addition, an outlook is given by creating a heat map for the warmest climate scenario in 2050 [22]. Wageningen serves as a testbed, since traverse meteorological measurements were available for a validation.

This paper is organized as follows: Section 2 summarizes the model approach of the heat map, Section 3 presents the results and validation and in section 4 and 5 we discuss and conclude our outcomes and modelling approach. A complete step-by step recipe is attached in the Supplementary Material.

2. Methods

Here, we present the description of the empirical PET-model which determines the important components that the heat map consist of in section 2.2. Thereafter in section 2.3 the calculation of these components is described in distinct steps, including the required geographical information datasets. Finally, we present the methodology to create a heat map according a future climate scenario and the methodology for the validation of traverse measurements.

2.1. Large town Wageningen as testbed

Wageningen is a large town with 39.673 inhabitants (2020) in the middle of the Netherlands [23] (see Fig. 1). The town is located at the edge of a shallow valley in the west and the slightly sloping nature area Veluwe in the east. On the south Wageningen is bordered by the river Rhine. The built-up area of the town contains about 2.5×2.5 km^2.

Fig. 1 indicates two important reference weather stations that will be used in this study. Wageningen University's weather station The Veenkampen (Fig. 1a) was used for the initial development of the recipe and verification of the standardized heat map. Since this weather station is located only 3 km from where the traverse measurements have been taken, we expect minimal errors in the heat map. To facilitate the development of future heat maps for other urban areas in the Netherlands, we advise to use nearby representative KNMI weather stations, which are easily accessible and equally formatted. All presented heat maps for Wageningen are driven by the closest representative KNMI station, which is KNMI station Herwijnen (WMO code 06356) Notwithstanding, it is noticed that the Veenkampen station meet the WMO requirements and it is located in an open rural area.

2.2. The empirical PET-model

Humans experience heat by registering the skin temperature and the blood temperature in the brains. The human body temperature is, apart from the meteorological conditions, also influenced by the internal heat production, sweat rate and clothing. These are personal and will vary substantially between the human activity outside [24], and is climate
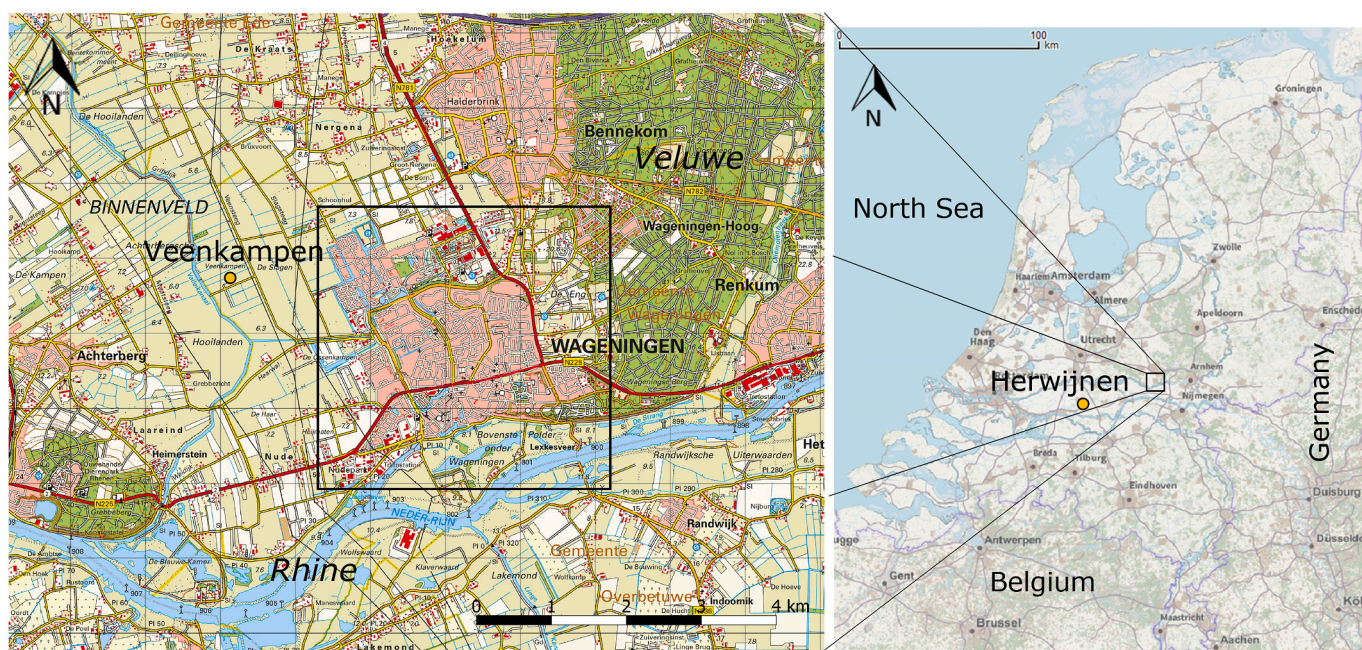

Fig. 1. The surroundings of the town Wageningen (panel A) and an overview map of the Netherlands (panel B). The black rectangle in panel A indicates the size of the calculated heat map. In panel A the weather station De Veenkampen (51.981°N, 5.620°E) is indicated and in Panel B the reference station Herwijnen is indicated.

zone dependent [25]. However, for policy making, it is important to use a standardized person, to fairly compare outside thermal conditions. For PET, this standardized person is male, 35 years old, 1.75 m, 75 kg, a clothing factor of 0.9 clo and he has a metabolic rate belonging to walking with 4 km h^{-1} [26]. PET classes were constructed to define different grades of thermal perception [17]. A PET above 29 °C indicates moderate heat stress in a temperate climate as Western and central Europe. The PET limit of 29 °C marks the point that the majority of persons feel uncomfortable regarding heat stress [24,27].

The PET was computed by an human body energy balance model [21], which accounts for the regulatory physiological processes of the human body and the meteorological parameters influencing the fluxes. Especially radiation, is very complex since it varies in three directions. We distinguish between direct radiation from the unobstructed sun, and diffuse radiation when scattered by clouds, and multiple reflections from buildings. At the moment it is computationally impossible to calculate on a 1-m grid accurately the radiation components for a whole city. Therefore, we used the 3D energy model Rayman to simulate the PET for three summer periods (April–September) for 10 typical Dutch street configurations [21], consisting of equal height terraced houses on both sides of the road (Fig. 2). The street configurations are east west and vary in canyon width resulting in sky-view factor (S_{vf}) ranging 0.05 to 1 both for natural surface and impervious road surface.

Air temperature, solar irradiation, thermal radiation and wind speed were used as meteorological input, as observed at the nearby weather station De Veenkampen. Only hours with PET values exceeding 20 °C were used as meteorological input to target for heat stress situations. The Rayman results were used to train an empirical PET model, based on regression techniques and meteorological and geographical data as input variables. In fact, two regression models have been developed, one for sunlit conditions and one for shadowed and nighttime conditions.

For sunlit conditions the resulting PET equation denotes:

$$PET_{sun} = -13.26 + 1.25T_a + 0.011Q_s - 3.37\ln(u_{1.2}) + 0.078T_w + 0.0055Q_s \ln(u_{1.2}) + 5.56\sin(\phi) - 0.0103Q_s \ln(u_{1.2}) \sin(\phi) + 0.0546B_b + 1.94S_{vf} \quad (1)$$
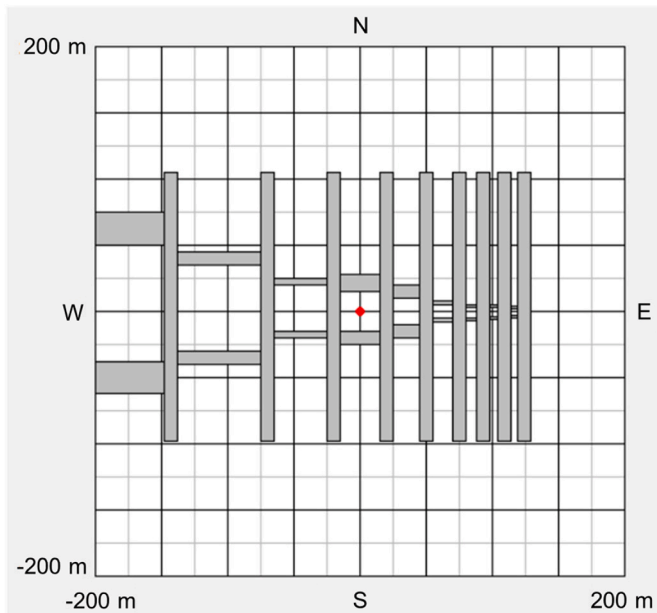
And for shadow and nighttime conditions:

Fig. 2. Representation of street configurations (grey bars) in human energy model Rayman. All walls are 10 m high and their albedo is 0.3. The resulting S_{vf} varied in successively steps from: 1.0, 0.809, 0.740, 0.620, 0.525, 0.373, 0.205, 0.152, 0.108 and 0.05.

$$PET_{shade, night} = -12.14 + 1.25T_a - 1.47\ln(u_{1.2}) + 0.060T_w + 0.015S_{vf}Q_d + 0.0060(1 - S_{vf})\sigma(T_a + 273.15)^4 \quad (2)$$

Herein T_a denotes the 2-m air temperature (°C), Q_s is the solar irradiation (W m^{-2}), $u_{1.2}$ is the wind speed at 1.2-m height (m s^{-1}), T_w the wet-bulb temperature, σ the Stefan Boltzmann constant (5.67.10^{-8} W m^{-2} K^{-1}), ϕ is the solar elevation angle (degrees), B_b Bowen ratio (ratio between sensible and latent heat flux), S_{vf} is the sky-view factor and Q_d the diffuse irradiation (W m^{-2}). For impervious urban surfaces a typical value of $B_b = 3$ was used and for well-evaporating vegetation B_b was set to 0.4 [28]. The used Bowen ratio is applicable for grass vegetation that can evaporate well (Bowen ratio for potential evaporation is about 0.3 [15], and this can be found at many times in deltas with relatively stable water tables in the western part of the Netherlands. The wind speed and air temperature are different for urban areas compared to the open rural reference station due to the differences in roughness and the UHI effect which methods is described in sections 2.3.1 and 2.3.2.

2.3. Mapping

The PET model of Eqs. (1) and (2) allows one to compute a heat map for the surroundings of the rural reference station mainly intended for urban areas but not limited to urban areas only. Hence, geographical or meteorological data must be processed to estimate the different components of these equations, which is presented in the flow diagram in Fig. 4 and Table 1. In case of the air temperature and wind speed, meteorological and geographical data has to be combined. We discuss the estimation of the components governing the PET mapping, i.e. air temperature and humidity effects, wind speed, and shade effects by buildings and trees.

2.3.1. Air temperature and wet-bulb temperature

The UHI depends on meteorological conditions and the density of the urban environment. Typical weather leading to high UHI are low wind speeds and sunny conditions. The daily maximum UHI (UHI_{max}) can be estimated by a diagnostic equation, which includes geographical - (left) and meteorological factors (right) [20]:

$$UHI_{max} = \left(2 - S_{vf} - F_{veg}\right) \sqrt[4]{\frac{S^\downarrow * (T_{max} - T_{min})^3}{U}} \quad (3)$$

Herein S_{vf} and F_{veg} are the spatially averaged sky-view factor, and vegetation fraction respectively with a certain source area (see Fig. 5). The meteorological term contains $S^\downarrow$, mean downward shortwave radiation (in Kms^{-1}) (kinematic units), $T_{max} - T_{min}$, the maximum – and minimum temperature (°C) representing the diurnal temperature range and U the mean wind speed (ms^{-1}), all measured at the rural reference station. T_{max} and T_{min} are determined between 8:00 UTC current day – 7:00 UTC next day (10:00–9:00 h local time) to represent the cooling potential outside the city [20]. The mean wind speed was also determined over this period. The mean downward short-wave radiation is determined over the current day. The maximum UHI occurs about 4 h after sunset for calm clear days [15,29]. For the other hours, the UHI$_{max}$ is diminished by a correction factor that varies between −0.02 and 1 in the diurnal cycle (Eq. (4), Tables S.3 and S.4 in Supplementary Material).

$$T_a[h] = T_{refstation} + UHI_{max} * diurnal\_cycle[h] \quad (4)$$

The diurnal cycle is inspired by a characteristic curve of UHI by Oke [15]. This curve was defined for one particular day length. For other day lengths the curves were adjusted considering that the minimum UHI occurs about 4 h after sunrise [30].

In the derivation of Eq. (3), it was implicitly considered that the remaining fraction of F_{veg} is built-up area [20]. Apart from the morphological effects described by the S_{vf} this built-up area is on average warmer due to the larger partitioning of sensible heat flux compared to the latent heat flux and has a temporal shift due the heat
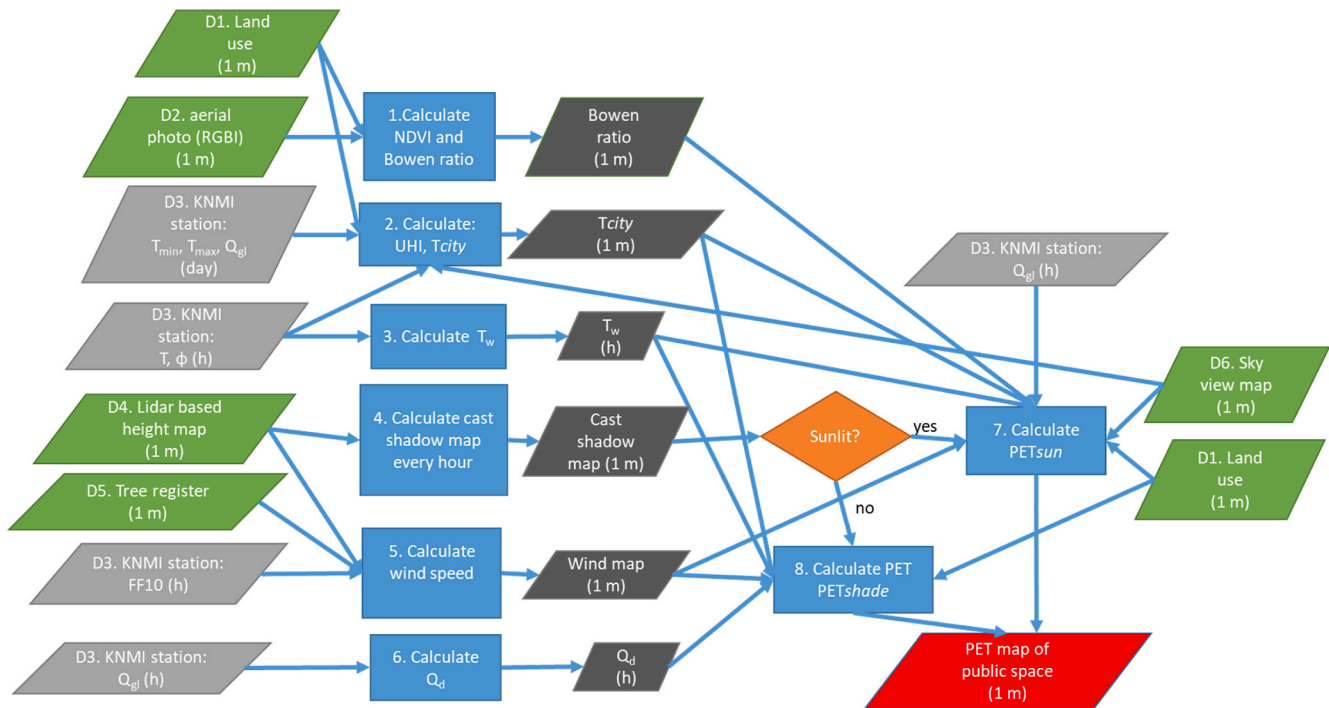
Fig. 3. Flow chart of the data sources (D), subdivided in maps (green) and temporal weather data (grey). The intermediate products are indicated in dark grey and actions are indicated in blue rectangles. The end product in this flow chart is the PET map (red). (For interpretation of the references to colour in this figure legend, the reader is referred to the Web version of this article.)
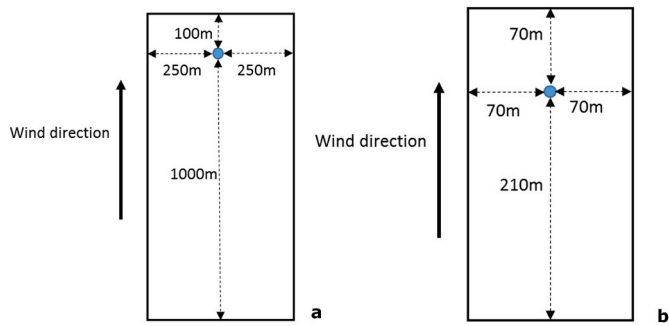

Fig. 4. (a) Source area for which the average sky-view factor and vegetation fraction is calculated on a resolution of 25 m. (b) Source area for the calculation of frontal area density and building and tree heights which serves as input for wind speed computations.

storage. The presence of water surfaces complicates the application of this equation. On the one hand, water bodies have a high heat capacity like built-up area [31], but on the other hand do evaporate and have higher latent heat fluxes and consequently lower sensible heat fluxes averaged over the day. To enable the applicability of the straightforward equations, water surfaces are treated as built-up area at night, and as vegetation at daytime. This temperature pattern is observed for a weather station in the harbour of Rotterdam [18].

The S_{vf} and F_{veg} were averaged for a source area of 500×1100 m (Fig. 4), which corresponds to the correlation of land use and urban temperature as found in Heusinkveld et al. [18]. The source area is oriented towards the wind direction. In case of low wind speeds (<1.5 ms^{-1}) a square-shaped source area of 700×700 m is used around the calculated grid cell. Since S_{vf} and F_{veg} are averaged over a large source area, the output resolution was set to 25 m to reduce computational costs.

To assign the F_{veg} two maps are created, one for daytime and one for nighttime, due to the special role of water surfaces. The vegetation

Table 1
Overview of used data sources for calculating the heat map. The resolution used for the calculation steps is 1 m. The resolution of the source data is shown in brackets. The exact links can be found in Table S1 in the Supplementary Material.

Map	Resolution (m or h)	Flow-chart	Source	Open data?
Land use	1 (vector data)	D1	Buildings and Water map: OpenStreetMap via www. Geofabrik.de Vegetation: www.pdok.nl	Yes
Aerial photo (RGBI)	1 (0.25)	D2	www.pdok.nl	Yes
Rural reference station, KNMI or Wageningen Univ.	1	D3	www.knmi.nl www.met.wur.nl/veenka mpen/data	Yes
Lidar based height map	1 (0.5)	D4	www.ahn.nl	Yes
Tree register	1 (vector data)	D5	www.boomregister.nl	No
Sky-view factor map	1	D6	www.knmi.nl	Yes

fraction per grid resolution is determined using NDVI <0.16 in the aerial photography. However, cropland might not be classified as vegetation fraction then, especially when it is bare at the time of data collection. Cropland, even if it is bare, will not store the amount of heat as built-up area does. Therefore, cropland is assigned as vegetation fraction in the computation of air temperature (Table S1 D1 bgt_begroeidterreindeel in Supplementary Material).

For the S_{vf} (either 1-m resolution for PET equation as 25-m resolution for T_a), water surfaces and buildings need to be excluded. A S_{vf} cannot be identified for water bodies, which is a limitation of the underlying lidar technology [32]. To estimate T_a, the S_{vf} under trees and other vegetated surfaces has been excluded. The effect of reduced S_{vf} in an urban canyon (mainly consisting of impervious road and pavements) has a more enhanced UHI effect than the reduced S_{vf} in parks by trees, due to the storage difference between buildings and trees. Ignoring the S_{vf} from
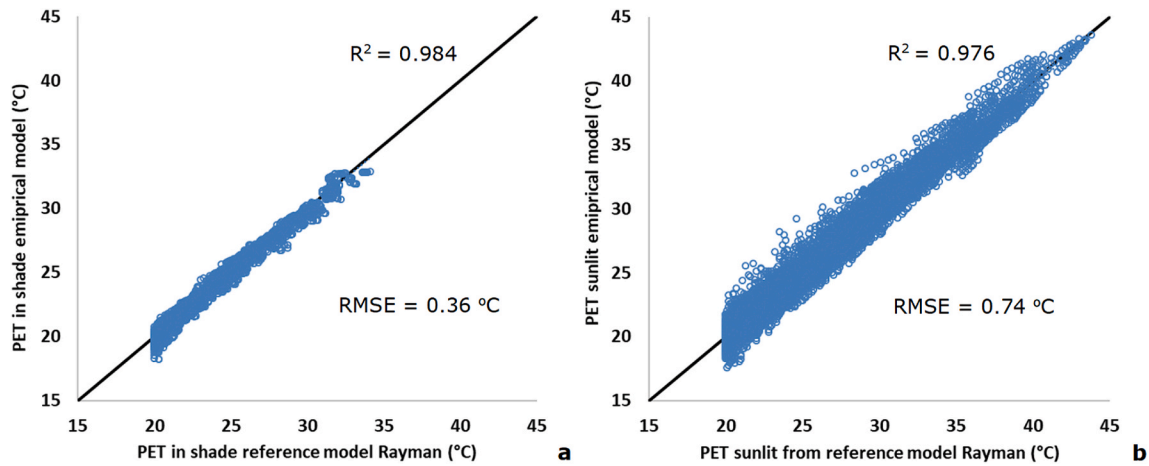
Fig. 5. Comparison between results of the empirical PET model and the reference output from human thermal energy model Rayman for (a) sunlit conditions and (b) shadowed conditions.

green surfaces cancels a large part of this uncertainty. Subsequently, the mean S_{vf} is computed over the source area. In case the vast majority is filtered out, then the S_{vf} is set to 1 corresponding the rural reference case. The specific rules are presented in the Supplementary Material chapter B2.

The wet-bulb temperature was calculated according to Ref. [33]:

$$T_w = T_a \, atan(0.151977(\varphi + 8.313659)^{0.5}) + atan(T_a + \varphi) - atan(\varphi - 1.676331) + 0.00391838\varphi^{1.5} \, atan(0.023101\varphi) - 4.686035 \quad (5)$$

Herein T_a denotes the air temperature and φ the relative humidity, both measured at the rural reference station. So, a constant T_w is applied everywhere including the city. The relatively small coefficients of T_w in Eq. (1) (6% compared to T_a), justifies this pragmatic approach, instead of calculating T_w for every urban grid cell with urban temperature. Besides, the relative humidity is generally lower in urban areas [34,35], which counteracts the slight rise on T_w due to higher urban air temperatures.

2.3.2. Wind speed

According to WMO guidelines reference weather stations were sited in open terrain with a low surface roughness [36]. The surface roughness is substantially higher at other locations in the heat map in the vicinity of buildings and trees which coincides with lower wind speeds. A translation of the wind speed was made from the open reference station to locations with a higher surface roughness. First, we computed the mesowind at the blending height (60 m) from the wind and surface roughness of the weather station (roughness length $z_0 = 0.03$ m) using a logarithmic wind profile in neutral conditions. The blending height is where the wind flow is supposed to be homogenous and thus independent of z_0. According to field experiments performed by MacDonald et al. [37], the wind speed is translated to 1.2 m in the urban canopy and representative for an averaged wind speed at neighbourhood scale. Above the roughness layer the wind profile is semi-logarithmic, whereas the wind profile is exponential within the urban canopy. A step-wise approach with equations is presented in the Supplementary Material chapter B5).

For the MacDonald method, the frontal area density of buildings is an important indicator of wind reductions in urban areas. The frontal areas were determined by deriving the perpendicular surfaces towards the wind direction (see Supplementary Material Fig. S.4 for a visual representation). The source area for the frontal area density is 280 * 140 m aligned in the wind direction (Fig. 4b).

Here we added the implementation of frontal area density of trees to compute a total frontal area density in Eq. (6), because trees also slow down the wind in real urban situations. The frontal area density for trees

is represented as if it was a rectangular shape (frontal view) which holds for ordinary buildings. The wind-oriented crown area consists of 55% of a rectangle λ surface, based on an ellipse shaped crown stretching 2/3 of the total height. Together with a small roughness reducing effect of porosity (0.9), the coefficient for trees 0.3 is half as large as the coefficient for buildings (0.6) (Eq. (6)). The offset 0.015 is used to account for a small saturation effect. Larger frontal areas have higher chances that buildings and trees stand in each other's wind shadow.

$$\lambda_{tot} = 0.6\lambda_{buildings} + 0.3\lambda_{trees} + 0.015 \quad (6)$$

The coefficients in Eq. (6) do not add up to 1, which is because often a part of the trees lies in the wind shade of adjacent buildings.

2.3.3. Sun and shadow

Exposure to direct sunshine is a prerequisite for high PET values. Sunlit locations can be determined by a cast shadow map. This cast shadow map can be created with the lidar based height map (AHN) and the UMEP GIS tool [38]. This GIS tool can calculate cast shadows at all solar elevation angles during the day and season. Unfortunately cast shadows cannot be determined at the surface under the tree crown. Therefore, the area below trees is designated as shadow if trees are higher than 2 m. This last prerequisite of 2 m is introduced to enable entering solar rays at the edge of the trees. In reality the foliage is partially transparent to solar radiation, so that PET values are slightly underestimated under trees. However, the priority is to distinguish the hot spots in the heat map which is never found under trees during day time.

The empirical PET equation in 2.1 require the solar irradiation (Q_s) and the diffuse irradiation (Q_d). The Q_d is calculated from Q_s as measured at the rural reference station, with a solar elevation angle (ϕ) that depends on the time of the day and the date:

$$\frac{Q_d}{Q_s} = \begin{cases} 1, & \text{if } \tau_a < 0.3 \\ 1.6 - 2\tau_a, & \text{if } 0.3 < \tau_a < 0.7 \\ 0.2, & \text{if } \tau_a > 0.7 \end{cases} \quad (7)$$

herein the atmospheric transmissivity (τ_a) is estimated as [39]:

$$\tau_a = \frac{Q_s}{1367 \, sin(\phi)} \quad (8)$$

The solar irradiation from the reference station is a sum of the past hour. To estimate the amount of radiation for the entire hour, the radiation for the coming hour and the past hour is averaged.

2.4. Climate scenarios

The recipe for the heat maps can also be utilized for climate projections. KNMI developed four scenarios for 2050 to depict how the climate may evolve [22]. These scenarios are derived from global climate model computations of the IPCC, global climate model EC-Earth results and on a downscaling step within a regional climate model. These model results are grouped in a scenario with a low - or high global temperature rise, and small – or large change in circulation pattern. For each scenario, KNMI provides numerical values for temperature, relative humidity and radiation shifts, allowing conversion of meteorological time series from the current to a future climate [40]. In this study we transformed the time series to the so called W_H scenario of 2050, which represents a high global temperature rise (W). The suffix "H" denotes a change in air circulation pattern, which envisages more high pressure dominance in summer resulting in drier, sunnier summers with an increase of easterlies. Daily maximum -, minimum - and average temperatures are transformed to the W_H scenario of 2050 and interpolated to hourly temperature values following Koopmans et al. [41], which further elaborates on Molenaar et al. [42].

We use a new hourly based transformation of radiation, which elaborates on the transformation of daily solar irradiation by Bakker [43]. In the W_H scenario, an increase in monthly radiation is expected due to a decrease in cloudiness in the summer months. It is important that already clear-sky sunny days will not receive extra radiation, since radiation is an important term in the PET. Therefore, the Angot radiation is determined on an hourly basis [44], and multiplied with a daily averaged transmission factor of the atmosphere as used in the Angstrom equation. For individual hours, a daily averaged transmission factor does not hold. At noon, the sun ray path through the atmosphere is shorter than just after sunrise and before sunrise. To estimate this difference, we created a series of measured ratio of solar irradiation/Angot radiation for the different hours for 15 summer half years. Per hour we created a 95-percentile. For the Netherlands this percentile represents days with unobstructed sunshine. Hours that receive this amount of radiation or more in current climate, cannot receive extra radiation in a future climate. For hours below the 95-percentile the projected radiation increase is applied with an upper limit of the 95-percentile. So, this procedure ensures a realistic transformation of radiation on an hourly basis and this is summarized in the conditional equations below (Eq. (9)). The values of the percentiles to calculate $Q^a(h)$ is presented in the Supplementary Material chapter B9, based on the climatology of reference weather station Herwijnen.

$$Q^f(h) = \begin{cases} Q^c(h), & \textbf{if } Q^c(h) > Q^a(h) \\ Q^a(h), & \textbf{if } Q^c(h) * Q^a(m) > Q^a(h) \\ Q^c(h) * Q^c(m), & \textbf{else} \end{cases} \qquad (9)$$

$Q^c(h)$ = hourly Q_s current climate
$Q^f(h)$ = hourly Q_s future climate
$Q^a(h)$ = Angot radiation corrected for 95-percentile of observed Q_s
$\Delta Q(m)$ = monthly Q_s increment to future climate

2.5. Traverse measurements with cargo bicycle

The heat map has been validated against mobile observations consisting of all meteorological quantities that affect the human energy balance. The mobile measuring setup consists of a cargo bicycle that is equipped with short-wave and thermal radiation sensors, ventilated air temperature and humidity sensors and an ultrasonic anemometer, see Heusinkveld et al. [45]. The measurement consists of a pre-programmed route, extending 6 km through urban areas. The route has been designed such that they sample as much as possible contrasting neighbourhoods, such as neighbourhoods with terraced houses, multi-storey apartments and a forested quarter with detached houses. The wind observations have been corrected for the bicycle speed by means of wheel - and GPS speed measurements. Since the sensors have a certain inertia, observations should be averaged over a stretch of 20 m. Besides, the radiation sensors are separated on both sides of the driver to prevent measuring the driver himself, which means it is not possible to measure exactly on the square meter. However, variables such as temperature and wind speed also vary greatly over time, which means that validation of a heat map is only useful after spatial averaging. The model results are averaged over a stretch of 20 m, and 10 m in width. Curves and (near) stand stills for intersections have not been sampled. Curves have more uncertainty in wind speed estimates and source areas. Also, locations where the building stock dataset (documented in 2010) strongly differs from the real building stock at the moment of the observations (in 2013), have been eliminated to ensure a proper comparison.

3. Results

3.1. Validation

In the validation section the empirical model is compared with thermal energy model Rayman and the model results are validated with cargo bike observations. We find a sound agreement between the empirical model and Rayman (Fig. 3). The deviations for the sunlit empirical model shows a little more spread, with a RMSE of 0.74 °C compared to an RMSE of 0.36 °C for shadowed empirical model.

The validation with observations and corresponding heat map is presented for August 2, 2013, which was a clear-sky warm summer day for which traverse measurements were available. The maximum temperature recorded at the rural site was 34.2 °C, and the afternoon background 10-m wind was 3 Bft (5 m/s). This day is comparable in temperature with the 1:1000 heat day presented in the next section.

Figs. 6 and 7 present respectively the modelled and observed PET and the difference between the modelled – observed PET for 12:00 UTC for urban areas. The relatively cool areas in the forested quarter in the northeast are well represented (white circle Fig. 7). In the city itself deviations in PET are larger, consisting of mainly positive biases. Fig. 8 shows the correlation between modelled and observed PET, especially in the higher PET percentiles with relative small standard deviations. The coefficient of determination is quite good with 0.656. The bias is 1.33 °C and the bias corrected RMSE amounts to 2.63 °C. In the lower and mid percentile groups (0.2–0.6) the differences are larger with a positive bias (median) that correspond to shadowed or partially shadowed locations. Most of these sampled locations have trees providing shade and the differences are directly linked to differences in observed and modelled radiation. Substantial differences occur in the real tree crown providing shadow and the tree crowns used in the model. PET differences between neighboring shadow and sunlit data points are ≅ 13 °C in the city and this can have a significant effect in the sampled source area. E.g. in the orange circle (Fig. 7) positive PET biases are caused by an overestimation of sunlit data points in the middle of the road. In the method, we used a 2-m object height threshold (lidar based) to remove edges of trees and defoliated trees. This operation leads to an overestimation in modelled radiation here and on average for the whole route. However, although PET biases are much smaller by renouncing this operation this leads to too low radiation averages near trees and a larger bias corrected RMSE. Besides, we note that there is a general uncertainty in the transmissivity of radiation of trees, especially in the diffuse component for foliated trees [46]. During droughts there is a larger risk of defoliation by insect defoliators and pests [47], which logically increase the transmissivity of radiation. In general, the variation of multiple reflections between buildings, street surface differing in albedo and trees in different configurations cannot be covered in its full complexity. The PET equation can resolve a part, based on the street configurations in the training dataset.

In Wageningen the average modelled wind speed corresponds well with the observations (bias amounts to 0.18 ms^{-1}). The spatial wind variation of the cargo bike and model does not match so well. From the

Fig. 6. Heat maps of modelled (left) and observed PET (right) on August 2nd, 2013 12:00 UTC (14:00 h local time).

observation side, uncertainties in wind speed arise through wind modifications by traffic and in lesser extent stream flow by the cargo bike and driver itself. More important, the wind speed is variable at short time scales because of daytime turbulence, and higher or lower wind observed wind speed may not always reflect the general wind speed at certain locations. From the model side, the urban wind is discussed in section 4. Wind speed differences are about three times less important in explaining the PET deviations than radiation differences. Finally, the modelled urban air temperature resembles the measured air temperature. The spatial differences in urban temperature are small at this time step, because the UHI is small in afternoon.

3.2. PET heat map for daytime

For the standardized PET map, we selected July 1, 2015, which is the 1:1000 heat day for WMO reference station Herwijnen (38 km southwest of Wageningen, Fig. 1b) for the period April–September. This corresponds to a 1 in 5.5 chance for the current climate. Also this day had continuous clear-sky weather with slightly more wind in afternoon, 3–4 Bft at the reference station. The afternoon average PET heat maps are shown in Fig. 9 for the current climate and for the future climate (KNMI '14 W_H scenario 2050).

Hot spots with 44 °C < PET<46 °C are found on locations facing many hours of sun during afternoon and where the wind is reduced due to large frontal area densities of buildings. Examples of such locations are relatively open spaces like squares and non-vegetated roundabouts (red circle 1 in Fig. 9a). Less open spaces as street canyons with middle-rise buildings, and downwind the urban centre with a large area of buildings and narrow streets are also hot spots (see red circles 2 and 3 in Fig. 9a). The coolest spaces at daytime are the locations under the trees in the shadow. Other relatively cool spaces that are sunlit are open places with much ventilation such as open parks (blue circle 1). Remarkably, also a crossing leeward of an impervious bus station is relatively cool (blue circle 2). Upwind there are only few buildings that aligned as such that the wind is not obstructed much.

The increase in PET in the W_H scenario amounts to 2.8 °C all over the map and can be almost entirely attributed to the change in background air temperature, so changes in urban-rural differences and changes in shade-sun differences are negligible (Fig. 9b). In other words, the magnitude of UHI is virtually unchanged in this scenario. The increase of sun duration is expected in the summer months for the W_H scenario and therefore solar irradiation increases on average. However, the selected

day was already sunny and significant increases in solar irradiation are therefore not possible. the W_H scenario is slightly drier in the summer months by adding the monthly numerical values. However, the lower relative humidity in the W_H scenario has a negligible effect on PET (0.04 °C).

3.3. PET exceedance map

From a climatological perspective it is interesting to examine an entire summer season of spatial PET differences. As climate stress tests should be focussed on heat stress, we may count the number of hourly exceedances of a PET threshold where most persons feel dissatisfied regarding heat stress, i.e. 29 °C. A PET exceedance map is robust since it is not influenced by day-specific weather. In the Netherlands warm episodes can originate from different circulation types [48], varying from weak winds from a central European high, or a stronger circulation of warm air from the south or east. To cover both mechanisms the accumulation of heat load over a whole summer is more representative than for a selected day. An analogous approach is used for moderating air quality in the European Union, whereby daily contaminant concentration exceedances are counted above a threshold value [49]. For contaminants, there is also a limit indicating the number of days per year this threshold value may be exceeded, which is not regulated for heat stress.

The exceedance maps show the number of hours the PET exceeded (PET> 29 °C) for the current climate and translated into the future climate (Fig. 10). The summer half year of 2013 has a climatological average temperature and average heat production (accumulation average daily temperatures above 18 °C) and is therefore representative as example.

Fig. 10a shows that in the town, the PET criterion was exceeded by $\cong$ 160 h per year in the rural countryside up to 430 h in wind sheltered and unshaded locations places. For the W_H scenario, an increase of 80–110 PET exceedance hours is expected for predominantly unshaded places. Locations with a relatively high shade and/or windy locations show a smaller increase i.e. up to a 30-h increase under trees.

4. Discussion and recommendations

4.1. Urban climate maps

Here we discuss heat maps developed with various models of

Fig. 7. Difference between modelled and observed PET on August 2nd, 2013 12:00 UTC, (14:00 h local time). The white circle indicates the forested quarter which is simulated well. The orange circle indicates a place with a positive PET bias induced by an overestimation of modelled radiation. (For interpretation of the references to colour in this figure legend, the reader is referred to the Web version of this article.)

contrasting complexity and grid spacings from 5 m to 500 m and compare these with our heat map. First, the urban heat maps are discussed which are based on general urban classifications and/or predominantly analytical or statistical geo-information models for landscaping a wind. Second, the heat maps based on complex numerical simulations are evaluated.

In the field of urban planning a popular method to distinguish distinct local climates is the use of climatopes [50]. Climatopes are urban classifications based on common climatic geographical aspects. Examples include the Thermal Environmental Map of Tokyo [51], and urban climatic maps for Hong Kong and Arnhem (UCMAPS) [52,53]. The Thermal Environmental map of Tokyo distinguishes different thermal classes on 500-m resolution based on urban density and anthropogenic heat, apart for residential and commercial areas [51,54]. Although this map may be intuitive and clear to urban planners they miss spatial detail and lacks heat stress criteria which is provided by our heat map.

The urban climatic map of Hong Kong contains more spatial detail and is also based on the PET estimated with continuous urban morphology data, green spaces and wind [53,54]. However, the map does not visualise PET but an urban classification scale. In contrast to our heat map, they did not take into account sun and cast shadow effects, which apparently is important for fine grid PET calculations. Another widely used methodology are the Local Climate Zone (LCZ) based on a scale of 250 m and larger. The LCZ differs from climatopes by leaving out local topography and local climatology factors [55], i.e. it will not represent wind ventilation paths. They are based on universally recognized built forms and land cover types and may serve well as basis for heat maps scaled up from neighbourhood observations [56], and numerical model heat maps [57,58]. Verdonck et al. [59] carried out both numerical simulations and an observational assessment on LCZ classes and found quite overlapping normalized temperature ranges.

Alternatively, Shi et al. [60] interpolated urban observations with different geographical mapping methods into an urban climate map and noted a RMSE for PET of 2.0–2.3 °C for Hong Kong. This compares well with the found RMSE in our study.

The finer scale heatmaps from numerical simulations which use a grid resolution between 100 m and 1 km [61–64] cannot capture the energy and wind flow of individual buildings and therefore it needs to parameterize. For urban parameters as building height and frontal area index the determination for a grid is comparable as calculated by the source areas in our study [61,63]. Although the offered detail is not so large for a heat map, the simulated temperatures were within an accuracy range of 1–2 °C for Bohnenstengel et al. [61]. Ronda et al. [63] evaluated urban fine-scale forecasting for lead times up to 48 h. Mean absolute errors from independent air temperature observations were quite low in the first 24 h, with 1.5 °C at day time and 1 °C at nighttime. Relatively small-scale models with grid spacings of ~5 m apply computational fluid dynamics, which implies that individual buildings with accompanying wind flow and energy exchanges could be resolved. Ashie et al. [65] performed a heat map for whole Tokyo with an RMSE of 1.1 °C. However, it should be noted that they used a steady state calculation since the size of the domain is huge. Although numerical models might perform slightly better than the analytical and statistical geo-models including ours, the applicability of the latter is larger to other areas. Moreover, the calculations of climate adaptation measures in the urban climate map is much faster for geo-models. Finally, it was demonstrated for our climate map that it is possible to calculate a climatology for a year, which is impossible for numerical models with a fine resolution for a city domain.
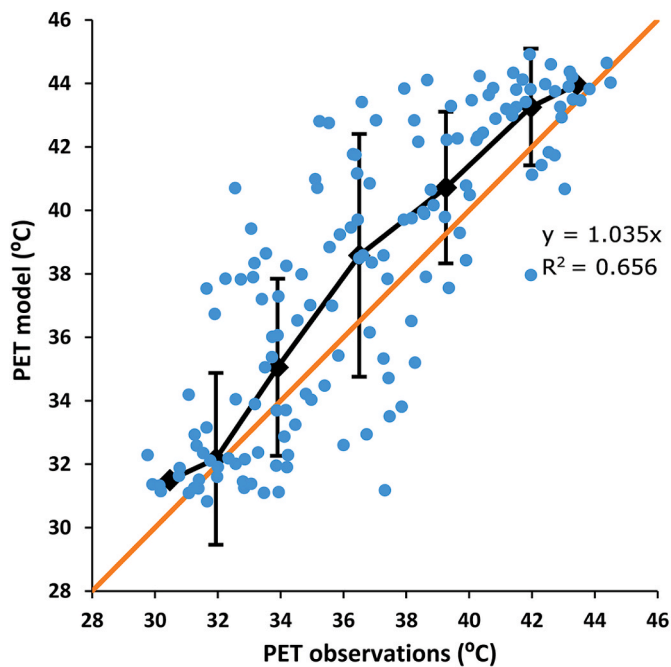
Fig. 8. Scatter plot of observed and modelled PET samples on August 2nd, 2013 at 12:00 UTC in Wageningen (blue dots). The black line and points indicate the percentile groups of the PET bike with bars indicating the standard deviation of PET differences between model and observation. The borders of the PET percentile groups are 0.05, 0.2, 0.4, 0.6, 0.8, 0.95. The lowest and highest percentile group <0.05 and >0.95 did not show a standard deviation, because the amount of data is limited compared to the other percentile groups. The orange line indicates the 1:1 line. (For interpretation of the references to colour in this figure legend, the reader is referred to the Web version of this article.)

4.2. Urban wind

Wind speed strongly affects the PET, because it determines largely how efficient the human body can transfer heat to the atmosphere [16]. Especially in situations with low wind speed, the PET is relatively sensitive to the wind speed as this can be observed in the logarithmic terms in the PET equation. So, the uncertainties in wind speed lead to a larger deviation in PET at low wind speeds.

Pedestrian wind speeds have also been derived with urban morphology by Johansson et al. [66], who found good statistical scores based upwind fetch distances to closest buildings and downwind S_{vf}. A downside is that trees are not implemented and that the set up and that the validation is done against another model instead of independent observations. The role of trees on the wind speed in urban canyons has been investigated by several studies [67–71]. Huang et al. [68] produced a straightforward regression equation translating open field wind velocities to urban site wind velocities by conducting one total canopy (planar surface) density from buildings and trees data from Heisler [69].

In addition, Kent et al. [67] earlier adopted vegetation frontal area densities in the morphometric method of MacDonald et al. [72] to calculate urban canopy wind. They expand the method by recalculating the z_0 and using separate drag coefficients for trees and based on porosity estimations of Guan et al. [73]. The relative contribution of trees in the frontal area density is similar (45%) to our estimations, holding the same dimensions of trees. Alternatively, Kent et al. [67] add the frontal area densities of trees to an unaltered definition of frontal areas for buildings. On the contrary, we reduced the contribution of buildings by a factor 0.6 (Eq. (6)), so our frontal area densities are smaller which correlates with less wind reduction.

With small-scale computational fluid dynamics models, wind speeds can be properly modelled around individual buildings and trees on a 1-m scale resolving turbulence [70]. However, the domain size is limited,

since the method is computationally intensive. Salim et al. [70] simulated a wind field for a domain size of 2 by 2 km^2 on 1-m scale for the city centre of Hamburg. A large city as Tokyo (33×33 km^2) has been simulated on 5-m resolution. Another advantage of the GIS-based tools approach in our study is that it allows for quicker computation of modifications in an urban area like greening or implementation of extra trees.

In the current approach, the source area for wind including the frontal area density is 280 * 140 m, aligned in the wind direction (Fig. 4b). Ching et al. [74] used 1 km^2 as resolution for frontal area density in NUDAPT, which is a database with urban morphology statistic set up for meteorological models. Wong and Nichol [75] and Burian et al. [76], used a smaller source area of 100 m. Although Wong and Nichol [75] finds a good correlation of 0.57 for modelled and observed windspeed in Hong Kong, we think 100 m is too small to estimate the wind speed. Firstly, local wind behaviour, like channel flow can be resolved partly with our approach and corner accelerations are not possible. Second, winds at higher levels, such as at the top of the roughness layer are affected by roughness elements further upstream [77]. The top of the roughness layer varies within urban morphologies differing in density and building height. Kent et al. [67] used this weighted source area approach for determination of roughness variables to calculate λ for a climatology of Swindon UK. Applied to Wageningen (similar urban density), our stationary source area covers 80% of the weighted source area, which corresponds well. Note that a larger source area for Wageningen would give excessive weight to obstacles further away.

4.3. Outlook and recommendations

Development and disclosure of reliable monitoring data regarding urban heat stress is of primary importance in order to better describe the influence of land use and urban morphology factors. Also fixed stations which measure the required components of the PET are indispensable. Validation with these stations may provide clarity about the skill of the PET heat maps, by comparing uncertainties due to temporal variations of wind humidity and temperature [60]. Geographical improvements in the heat map consists of applying thermal properties of the urban fabric including albedo, a more sophisticated approach incorporating water surfaces, and anthropogenic heat sources.

Starting with anthropogenic heat, this may be included in the UHI formula by adding it to the solar irradiation. Although it implies that not all terms on the meteorological of the formula is measured at a rural site anymore, physically urban specific energy fluxes can be applied here. Note, that the UHI equation is in the end a diagnostic regression formula between two dimensionless groups in a dimensional analysis. For most cities in Western Europe (where the equation has been tested) anthropogenic heat plays a minor role on hot summer days, compared to solar irradiation determining the UHI. For dense high-rise districts as the city of London and central Tokyo reporting summer daily averages over 100 Wm^{-2} [78,79], anthropogenic heat becomes more significant. For comparison warm sunny days denote typically 300–350 Wm^{-2} for mid-latitudes.

The albedo determines the fraction of solar radiation that is absorbed by a surface. For urban areas this determines also how much energy is stored in the urban fabric and relates directly to UHIs. Increasing urban fabric albedo by 0.2 can result in a daily peak reduction of 0.65 °C for a clear summer day based on validated model simulations for Basel, Switzerland [80]. In Eq. (3) the albedo can be included as an absorption coefficient in front of the solar irradiation term.

However, Eq. (3) will not account for direct effects of adjustments of albedo on air temperature at daytime, since at daytime the diurnal factor is small. It is more complicated to incorporate these effects in a practical formula. Different albedos lead also to different partition of incoming shortwave radiation reflected by walls and streets. Therefore, it is recommended to retrain the PET model with the human energy model
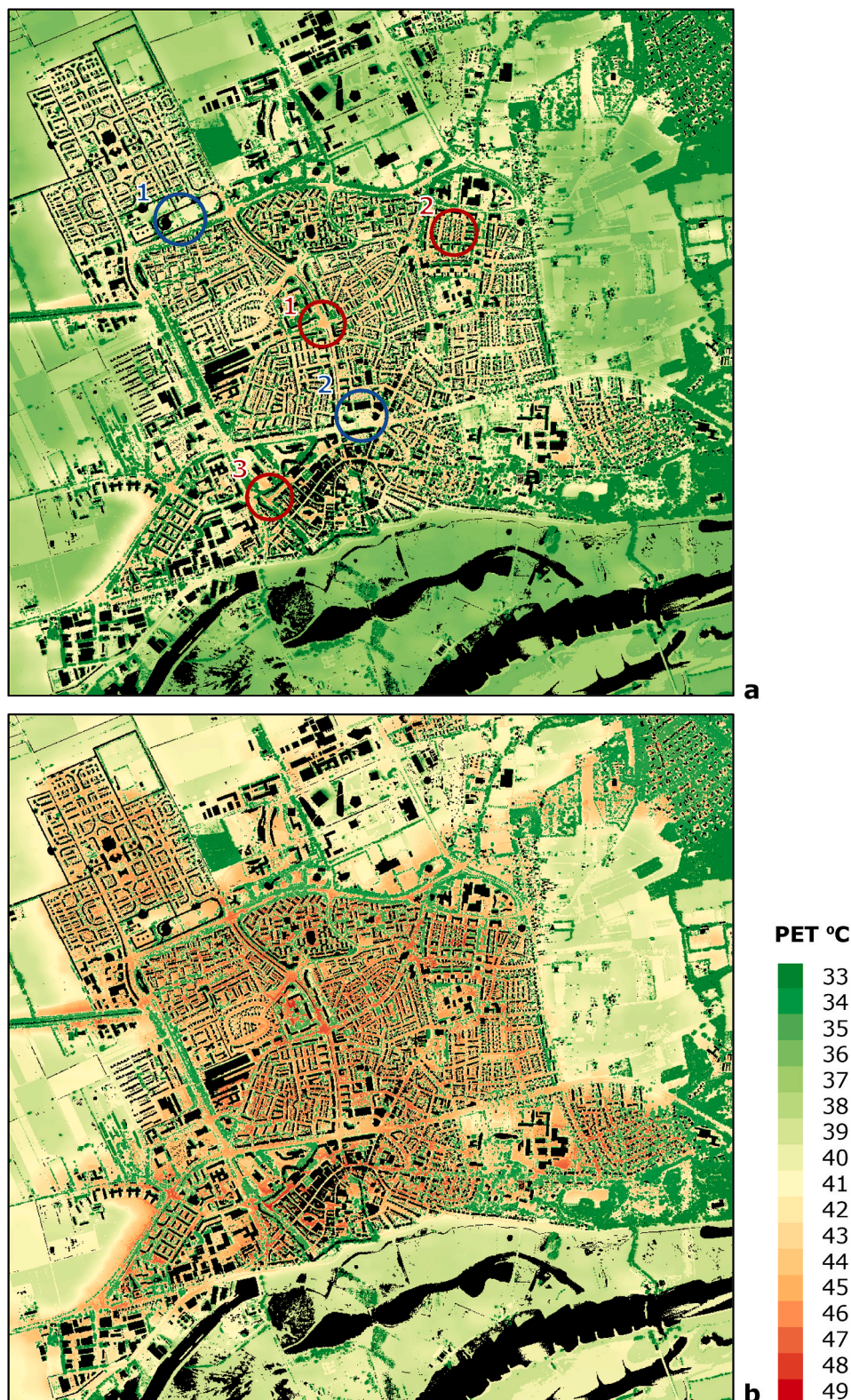
Fig. 9. Heat map showing mean PET for July 1st, 2015, during 10:00–16:00 UTC (12:00–18:00 h local time) driven with the meteorology of the Herwijnen reference station. (a) current climate, (b) future climate 2050, translation to the W_H climate scenario. Red circles indicate hot spots and the blue circle a cool spot. (For interpretation of the references to colour in this figure legend, the reader is referred to the Web version of this article.)

Rayman for various albedos. For both albedo and anthropogenic heat, it is advised to re-evaluate the underlying regression of the UHI equation and coefficients might be added to the meteorological variables. Furthermore, we like to address that soil moisture availability is important to consider. Dry episodes will reduce the cooling effects of vegetation by limiting evapotranspiration. It is recommended to apply higher Bowen ratios if soil moisture is limited. This is common for drier climates and sandy soils that is known to be unable to retain water well.

Fig. 10. Modelled number of hourly PET exceedances above 29 °C in 2013 for the current climate (a) and the W_H climate scenario (b) with the meteorology of the Herwijnen reference station.

In our study the soil moisture availability was quite high and relatively stable, because parts of Wageningen are a seepage area and water levels are managed in detail.

Finally, we discuss the empirical PET equation and the thermal thresholds. In other climate zones thermal perceptions may vary, due to the adaptation to a warmer or colder climate [25]. Also, the metabolic rates of equal activities vary and therefore the corresponding PET is different. The moderate heat stress limit in Taiwan is 5 °C higher compared to that of Western and central Europe [81]. Besides it is

important to retrain the PET model with representative climate data in other climate zones.

5. Conclusions

In this paper, we present a recipe for a 1-m resolution heat map representing the Physiological Equivalent Temperature (PET) at pedestrian height for current and future climate. As testbed the mid-sized town of Wageningen (the Netherlands) has been chosen since traverse

observations are available for this town. The heat map is developed in two stages. First, we derive an empirical PET model based on Rayman model simulations for a representative set of street configurations and through the summer season. Second, this empirical model is applied for a city using geographical information. Herein, established methods for estimating urban air temperatures and street-level winds are combined in an empirical PET-model.

Subsequently, one heat map is derived for a warm clear-sky summer afternoon which represents a 1:1000 heat day. By aggregating the PET load for the entire afternoon, the map represents an average heat load and justifies the hourly sun and shadow differences. The maximum PET in the afternoon amounts to 46 °C for calm sun exposed locations. In the KNMI W_H climate scenario for 2050 the PET is projected to increase quite uniformly with 2.8 °C. In addition, climatological heat doses are calculated by counting exceedances of PET values above 29 °C. For a representative year the masximum exceedances develop from 430 h to 530 h per year in the W_H scenarios. Within a city, the amount of exceedance hours is threefold that of the open rural environment. From a verification with cargo bike weather observations, radiation differences lead to largest uncertainties in PET, due to uncertainties in the size and transmissivity of tree crowns.

With this recipe for heat maps we intend to promote risk dialogues within municipalities and relevant boards. A logical next step is the development of a national PET heat map based on the developed recipe. Further progress can be made by including albedo, anthropogenic heat and a more sophisticated inclusion of water surfaces.

Declaration of competing interest

The authors declare the following financial interests/personal relationships which may be considered as potential competing interests:

Acknowledgements

Appendix A. Supplementary data

Supplementary data to this article can be found online at https://doi.org/10.1016/j.buildenv.2020.106984.

References

[1] IPCC, Impacts, Adaptation, and Vulnerability. Part A: Global and Sectoral Aspects. Contribution of Working Group II to the Fifth Assessment Report of the Intergovernmental Panel on Climate Change, Cambridge University Press, United Kingdom and New York, NY, USA, 2014.

[2] F. Hoeven van der, A. Wandl, Amsterwarm: mapping the landuse, health and energy-efficiency implications of the Amsterdam urban heat island, Build. Serv. Eng. Technol. 36 (1) (2015) 67–88, https://doi.org/10.1177/0143624414541451.

[3] Atlas natuurlijk kapitaal ([in Dutch]), http://www.atlasnatuurlijkkapitaal.nl/kaarten, 2020. (Accessed 5 May 2020).

[4] Climate Impact Atlas, 2020 accessed, http://www.klimaateffectatlas.nl/en/. (Accessed 5 May 2020).

[5] E.M. Fischer, C. Schär, Consistent geographical patterns of changes in high-impact European heatwaves, Nat. Geosci. 3 (2010) 398–403, https://doi.org/10.1007/s00484-018-1530-6.

[6] T. Pogačar, A. Casanueva, K. Kozjek, The effect of hot days on occupational heat stress in the manufacturing industry: implications for workers' well-being and productivity, Int. J. Biometeorol. 62 (7) (2018) 1251–1264, https://doi.org/10.1007/s00484-018-1530-6.

[7] A. Fouillet, G. Rey, F. Laurent, G. Pavillon, S. Bellec, C. Ghihenneuc-Jouyaux, Excess mortality related to the August 2003 heat wave in France, Int. Arch. Occup. Environ. 80 (2006) 16–24, https://doi.org/10.1007/s00420-006-0089-4.

[8] D. D'Ippoliti, P. Michelozzi, C. Marino, et al., The impact of heat waves on mortality in 9 European cities: results from the Euroheat Project, Environ. Health 9 (2010), https://doi.org/10.1186/1476-069X-9-37.

[9] A. Gasparrini, Y. Guo, F. Sera, A.M. Vicedo-Cabrera, V. Huber, S. Tong, M.S.Z. Coelho, P.H.N. Saldiva, E. Lavigne, P.M. Correa, et al., Projections of temperature-related excess mortality under climate change, Lancet. Planet. Health (2017) 360–367, https://doi.org/10.1016/S2542-5196(17)30156-0.

[10] M.T.E. Huynen, P. Martens, Climate change effects on heat- and cold-related mortality in The Netherlands: a scenario-based integrated environmental health impact assessment, Int. J. Environ. Res. Publ. Health 12 (2015) 13295–13320, https://doi.org/10.3390/ijerph121013295.

[11] J.F. Clarke, Some effects of the urban structure on heat mortality, Environ. Res. 5 (1) (1971) 93–104, https://doi.org/10.1016/0013-9351(72)90023-0.

[12] R. Basu, J.M. Samet, Relation between elevated ambient temperature and mortality: a review of the, Epidemiol. Rev. 24 (2) (2002) 190–202, https://doi.org/10.1093/epirev/mxf007.

[13] L. Grize, A. Huss, O. Thommen, C. Schindler, C. Braun-Fahrländer, Heat wave 2003 and mortality in Switzerland, Swiss Med. Wkly. 135 (2005) 200–205.

[14] B. Holmer, A simple operative method for determination of sky view factors in complex urban canyons from fisheye photographs, Meteorol. Z. 1 (5) (1992) 236–239, https://doi.org/10.1127/metz/1/1992/236.

[15] T.R. Oke, The energetic basis of the urban heat island, Q. J. R. Meteorol. Soc. 108 (455) (1982) 1–24, https://doi.org/10.1002/qj.49710845502.

[16] P. Höppe, The physiological equivalent temperature - a universal index for the biometeorological assessment of the thermal environment, Int. J. Biometeorol. 43 (2) (1999) 71–75, https://doi.org/10.1007/s004840050118.

[17] A. Matzarakis, M. de Rocco, G. Najjar, Thermal bioclimate in Strasbourg - the 2003 heat wave, Theor. Appl. Climatol. 98 (2009) 209–220, https://doi.org/10.1007/s00704-009-0102-4.

[18] B.G. Heusinkveld, G.J. Steeneveld, L.W. A van Hove, C.M.J. Jacobs, A.A.M. Holtslag, Spatial variability of the Rotterdam urban heat island as influenced by urban land use, J. Geophys. Res. Atmos. 119 (2) (2014) 677–692, https://doi.org/10.1002/2012JD019399.

[19] W. Klemm, B.G. Heusinkveld, S. Lenzholzer, M.H. Jacobs, L.W.A. van Hove, Psychological and physical impact of urban green spaces on outdoor thermal comfort during summertime in The Netherlands, Build, Environ. Times 66 (2015) 120–128, https://doi.org/10.1016/j.buildenv.2014.05.013.

[20] N.E. Theeuwes, G.J. Steeneveld, R.J. Ronda, A.A.M. Holtslag, A diagnostic equation for the daily maximum urban heat island effect for cities in Northwestern Europe, Int. J. Climatol. (2017), https://doi.org/10.1002/joc.4717.

[21] A. Matzarakis, F. Rutz, H. Mayer, Modelling Radiation fluxes in simple and complex environments – basics of the RayMan model, Int. J. Biometeorol. 54 (2010) 131–139, https://doi.org/10.1007/s00484-009-0261-0.

[22] A.M.G. Klein Tank, J. Beersma, B. Bessembinder, B. van den Hurk, G. Lenderink, KNMI'14 Climate Scenarios for the Netherlands; A Guide for Professionals in Climate Adaptation, KNMI Publication, 2015, p. 34. Brochure KNMI'14 Climate scenarios, De Bilt, http://www.klimaatscenarios.nl/brochures/images/Brochure_KNMI14_EN_2015.pdf. (Accessed 5 May 2020).

[23] CBS (Centraal Bureau voor de Statistiek) StatLine, Regionale Kerncijfers Nederland, 20 March 2020. https://opendata.cbs.nl/statline/#/CBS/nl/dataset/70072ned/table?ts=1574944489452. (Accessed 5 May 2020) ([in Dutch]).

[24] P.O. Fanger, Assessment of man's thermal comfort in practise, Br. J. Ind. Med. 30 (1973) 313–324, https://doi.org/10.1136/oem.30.4.313.

[25] P. Cohen, O. Potchter, A. Matzarakis, Human thermal perception of Coastal Mediterreanean outdoor urban environments, Appl. Geogr. 37 (2013) 1–10, https://doi.org/10.1002/joc.1330.

[26] Vdi, Methods for the Human Biometeorological Evaluation of Climate and Air Quality for the Urban and Regional Planning, Part 1: Climate. Beuth, Berlin, VDI Guideline 3787, Part 2, 1998.

[27] A. Matzarakis, H. Mayer, M.G. Iziomon, Applications of a universal thermal index: physiological equivalent temperature, Int. J. Biometeorol. 43 (1999) 76–84, https://doi.org/10.1007/s004840050119.

[28] T.R. Oke, Boundary Layer Climates, Routledge, London, 1987.

[29] J. Unger, Sümeghy, Á. Gulyás, Z. Bottyán, L. Mucsi, Land-use and meteorological aspects of the urban heat island, Meteorol. Appl. 8 (2001) 189–194, https://doi.org/10.1017/S1350482701002067.

[30] N.E. Theeuwes, G.J. Steeneveld, R.J. Ronda, M.W. Rotach, A.A.M. Holtslag, Cool city mornings by urban heat, Environ. Res. Lett. 10 (2015), 114022, https://doi.org/10.1088/1748-9326/10/11/114022.

[31] G.J. Steeneveld, S. Koopmans, N.E. Theeuwes, Refreshing the role of open water surfaces on mitigating the maximum urban heat island effect, Landsc. Urban Plann. 121 (2014) 92–96, https://doi.org/10.1080/00038628.2015.1105195.

[32] B.B. Worstell, S. Poppenga, G.A. Evans, S. Prince, Lidar Point Density Analysis: Implications for Identifying Water Bodies, U.S. Geological Survey Scientific Investigations Report 2014, Reston, Virginia, 2014, pp. 5191–5210, https://doi.org/10.3133/sir20145191.

[33] R. Stull, Wet-bulb temperature from relative humidity and air temperature, J. Appl. Meteorol. Clim. 50 (2011) 2267–2269, https://doi.org/10.1175/JAMC-D-11-0143.1.

[34] H.E. Landsberg, T.N. Maisel, Micrometeorological observations in an area of urban growth, Boundary-Layer Meteorol. 2 (1972) 365–370, https://doi.org/10.1007/BF02184776.

[35] K.D. Hage, Urban-rural humidity differences, J. Appl. Meteorol. 14 (1975) 1277–1283, https://doi.org/10.1175/1520-0450(1975)014<1277:URHD>2.0.CO;2.

[36] WMO, Guide to Meteorological Instruments and Methods of Observation. 2014 Edition WMO-No. 8, 2014. https://library.wmo.int/doc_num.php?explnum_id=4147. (Accessed 12 March 2020).

[37] R.W. MacDonald, Modelling the mean velocity profile in the urban canopy layer, Boundary-Layer Meteorol. 97 (2000) 25–45, https://doi.org/10.1023/A:1002785830512.

[38] F. Lindberg, C.S.B. Grimmond, A. Gabey, B. Huang, C.W. Kent, T. Sun, N. E. Theeuwes, L. Järvi, H.C. Ward, I. Capel-Timms, Y. Chang, P. Jonsson, N. Krave, D. Liu, K.F.G. Olofson, J. Tan, D. Wästberg, Z. Zhang, Urban multi-scale environmental predictor (UMEP): an integrated tool for city-based climate services, Environ. Model. Software 99 (2018) 70–87, https://doi.org/10.1016/j.envsoft.2017.09.020.

[39] W.C. Rooy, A.A.M. Holtslag, Estimation of surface radiation and energy flux densities from single-level weather data, J. Appl. Meteorol. 38 (1998) 526–540, https://doi.org/10.1175/1520-0450(1999)038<0526:EOSRAE>2.0.CO;2.

[40] KNMI, Toelichting Transformatie Tijdreeksen, KNMI, De Bilt, accessed, http://www.klimaatscenarios.nl/toekomstig_weer/transformatie/Toelichting_TP.pdf, 2015. (Accessed 5 May 2020).

[41] S. Koopmans, R. Ronda, G.J. Steeneveld, A.A.M. Holtslag, A.M.G. Klein Tank, Quantifying the effect of different urban planning strategies on heat stress for current and future climates in the agglomeration of the hague (The Netherlands), Atmosphere 9 (353) (2018), https://doi.org/10.3390/atmos9090353.

[42] R.E. Molenaar, B.G. Heusinkveld, G.J. Steeneveld, Projection of rural and urban human thermal comfort, Int. J. Climatol. 36 (4) (2016) 1708–1723, https://doi.org/10.1002/joc.4453.

[43] A. Bakker, Time Series Transformation Tool Version 3.1, Technical report; TR-349, KNMI, De Bilt, the Netherlands, 2015, p. 40, http://bibliotheek.knmi.nl/knmipubTR/TR349.pdf. (Accessed 5 May 2020).

[44] R.G. Allen, L.S. Pereira, D. Raes, M. Smith, Crop Evapotranspiration: Guidelines for Computing Crop Water Requirements - FAO Irrigation and Drainage Paper 56, FAO, 1998 accessed, http://www.scscourt.org/complexcivil/105CV049053/volume3/172618e_5xAGWAx8.pdf. (Accessed 5 May 2020).

[45] B.G. Heusinkveld, L.W.A. Hove, C.M.J. Jacobs, G.J. Steeneveld, J.A. Elbers, E. J. Moors, A.A.M. Holtslag, Use of a mobile platform for assessing urban heat stress in Rotterdam. Proceedings of the 7th Conference on Biometeorology Albert-Ludwigs-University of Freiburg, Meteorol. Inst., Univ. Freiburg, Freiburg, Germany, 2010, pp. 433–438.

[46] J. Konarska, F. Lindberg, A. Larsson, S. Thorsson, B. Holmer, Transmissivity of solar radiation through crowns of single urban trees—application for outdoor thermal comfort modelling, Theor. Appl. Climatol. 117 (2014) 363–376, https://doi.org/10.1007/s00704-013-1000-3.

[47] G. Rouault, J.N. Candau, F. Lieutier, L.M. Nageleisen, J.C. Martin, N. Warzée, Effects of drought and heat on forest insect populations in relation to the 2003 drought in Western Europe, Annu. For. Sci. 63 (2006) 613–624, https://doi.org/10.1051/forest:2006044.

[48] J. Kyselý, Influence of the persistence of circulation patterns on warm and cold temperature anomalies in Europe: analysis over the 20th century, Global Planet. Change 62 (1–2) (2008) 147–163, https://doi.org/10.1016/j.gloplacha.2008.01.003.

[49] EU-Commision, Directive 2008/50/EC of the European Parliament and of the Council of 21 May 2008 on ambient air quality and cleaner air for Europe, Official J. European Communities 152 (2008) 1–44.

[50] D. Scherer, U. Fehrenbach, H.D. Beha, E. Parlow, Improved concepts and methods in analysis and evaluation of the urban climate for optimizing urban planning processes, Atmos. Environ. 33 (1999) 4185–4193, https://doi.org/10.1016/S1352-2310(99)00161-2.

[51] TMG, Guidelines for Heat Island Control Measures, 2005. Tokyo, https://www.kankyo.metro.tokyo.lg.jp/en/about_us/videos_documents/documents_1.files/heat_island.pdf. (Accessed 5 May 2020).

[52] C. Ren, T. Spit, S. Lenzholzer, H.L.S. Yim, B.G. Heusinkveld, L.W.A. van Hove, L. Chen, S. Kupski, R. Burghardt, L. Katzschner, Urban climate map system for Dutch spatial planning, Int. J. Appl. Earth Obs. 18 (2012) 207–221, https://doi.org/10.1016/j.jag.2012.01.026.

[53] E. Ng, Towards planning and practical understanding of the need for meteorological and climatic information in the design of high-density cities: a case-based study of Hong Kong, Int. J. Climatol. 32 (2012) 582–598, https://doi.org/10.1002/joc.2292.

[54] C. Ren, E. Ng, L. Katzschner, Urban climatic map studies: a review, Int. J. Climatol. (2011) 2213–2233, https://doi.org/10.1002/joc.2237.

[55] I.D. Stewart, T.R. Oke, Local climate zones for urban temperature studies, Bull. Am. Meteorol. Soc. 93 (2015) 1879–1900, https://doi.org/10.1175/BAMS-D-11-00019.1.

[56] P.J. Alexander, G. Mills, Local climate classification and Dublin's urban heat island, Atmosphere 5 (2014) 755–774, https://doi.org/10.3390/atmos5040755.

[57] R. Basset, X. Cai, L. Chapman, C. Heaviside, J.E. Thornes, C.L. Muller, D.T. Young, E.L. Warren, Observations of urban heat island advection from a high-density monitoring network, Q. J. R. Meteorol. Soc. 142 (2016) 2434–2441, https://doi.org/10.1002/qj.2836.

[58] J. Ching, G. Mills, B. Bechtel, L. See, J. Feddema, X. Wang, C. Ren, O. Brousse, A. Martilli, M. Neophytou, P. Mouzourides, I. Stewart, A. Hanna, E. Ng, M. Foley, P. Alexander, D. Aliaga, D. Niyogi, A. Shreevastava, P. Bhalachandran, V. Masson, J. Hidalgo, J. Fung, M. Andrade, A. Baklanov, W. Dai, G. Milcinski, M. Demuzere, N. Brunsell, M. Pesaresi, S. Miao, Q. Mu, F. Chen, N.E. Theeuwes, WUDAPT: an urban weather, climate, and environmental modeling infrastructure for the Anthropocene, Bull. Am. Meteorol. Soc. 99 (2018) 1907–1924, https://doi.org/10.1175/BAMS-D-16-0236.1.

[59] M.L. Verdonck, M. Demuzere, H. Hooyberghs, C. Beck, J. Cyrys, A. Schneider, R. Dewulf, F. van Coillie, The potential of local climate zones maps as a heat stress assessment tool, supported by simulated air temperature data, Landsc. Urban Plann. 178 (2018) 183–197, https://doi.org/10.1016/j.landurbplan.2018.06.004.

[60] Y. Shi, C. Ren, Y. Zheng, E. Ng, Mapping the urban microclimatic spatial distribution in a sub-tropical high-density urban environment, Architect. Sci. Rev. 59 (5) (2016) 370–384, https://doi.org/10.1080/00038628.2015.1105195.

[61] S.I. Bohnenstengel, S. Evans, P.A. Clark, S.E. Belcher, Simulations of the London urban heat island, Q. J. R. Meteorol. Soc. 137 (2011) 1625–1640, https://doi.org/10.1002/qj.855.

[62] P. Hoffmann, R. Schoetter, H. Schlünzen, Statistical-dynamical downscaling of the urban heat island in Hamburg, Meteorol. Z. 27 (2) (2018) 89–109, https://doi.org/10.1127/metz/2016/0773.

[63] R.J. Ronda, G.J. Steeneveld, B.G. Heusinkveld, Urban finescale forecasting reveals weather conditions with unprecedented detail, Bull. Am. Meteorol. Soc. 98 (2017) 2675–2688, https://doi.org/10.1175/BAMS-D-16-0297.1.

[64] C. Heaviside, X.M. Cai, S. Vardoulakis, The effects of horizontal advection on the urban heat island in Birmingham and the WestMidlands, United Kingdom during a heatwave, Q. J. R. Meteorol. Soc. 141 (2015) 1429–1441, https://doi.org/10.1002/qj.2452.

[65] Y. Ashie, T. Kono, Urban-scale CFD analysis in support of a climate-sensitive design for the Tokyo Bay area, Int. J. Climatol. 31 (2) (2011) 174–188, https://doi.org/10.1002/joc.2226.

[66] L. Johansson, S. Onomura, F. Lindberg, J. Seaquist, Towards the modelling of pedestrian wind speed using high-resolution digital surface models and statistical methods, Theor. Appl. Climatol. 124 (2016) 189–203, https://doi.org/10.1007/s00704-015-1405-2.

[67] C.W. Kent, C.S.B. Grimmond, D. Gatey, Aerodynamic roughness parameters in cities: inclusion of vegetation, J. Wind Eng. Ind. Aerod. 169 (2017) 168–176, https://doi.org/10.1016/j.jweia.2017.07.016.

[68] Y.J. Huang, H. Akbari, H. Taha, The Wind-Shielding and Shading Effects of Trees on Residential Heating and Cooling Requirements, ASHRAE proceedings, Atlanta, USA, 1990, pp. 10–14. https://escholarship.org/uc/item/85g3s8xt. (Accessed 5 May 2020).

[69] G.M. Heisler, Mean wind speed below building height in residential neighborhoods with different tree densities, Build. Eng. 96 (1) (1990) 1389–1396.

[70] M.H. Salim, K.H. Schlünzen, D. Grawe, Including trees in the numerical simulations of the wind flow in urban areas: should we care? J. Wind Eng. Ind. Aerod. 144 (2015) 84–95, https://doi.org/10.1016/j.jweia.2015.05.004.

[71] L. Zhang, Q. Zhan, Y. Lan, Effects of the tree distribution and species on outdoor environment conditions in a hot summer and cold winter zone: a case study in Wuhan residential quarters, Build. Environ. 130 (2018) 27–39, https://doi.org/10.1016/j.buildenv.2017.12.014.

[72] R.W. MacDonald, R.F. Griffiths, D.J. Hall, An improved method for the estimation of surface roughness of obstacle arrays, Atmos. Environ. 32 (11) (1998) 1857–1864, https://doi.org/10.1016/S1352-2310(97)00403-2.

[73] D. Guan, Y. Zhang, T. Zhu, A wind-tunnel study of windbreak drag, Agric For. Meteorol. 118 (1–2) (2003) 75–84, https://doi.org/10.1016/S0168-1923(03)00069-8.

[74] J. Ching, M. Brown, S. Burian, F. Chen, R. Cionco, A. Hanna, T. Hultgren, T. McPherson, D. Sailor, H. Taha, D. Williams, National urban database and access portal tool, Bull. Am. Meteorol. Soc. 90 (8) (2009) 1157–1168, https://doi.org/10.1175/2009BAMS2675.1.

[75] M.S. Wong, J.E. Nichol, Spatial variability of frontal area index and its relationship with urban heat island intensity, Int. J. Rem. Sens. 34 (3) (2013) 885–896, https://doi.org/10.1080/01431161.2012.714509.

[76] S.J. Burian, M.J. Brown, S.P. Linger, Morphological Analyses Using 3D Building Databases: Los Angeles, California, Report LA-UR-02-0781, Los Alamos National Laboratory, Los Angeles, California, 2002, p. 73. https://www.researchgate.net/publication/260286741. (Accessed 5 May 2020).

[77] C.S.B. Grimmond, T.S. King, M. Roth, O. TR, Aerodynamic roughness of urban areas derived from wind observations, Boundary-Layer Meteorol. 89 (1) (1998) 1–24, https://doi.org/10.1023/A:1001525622213.

[78] T. Ichinose, K. Shimodozono, K. Hanaki, Impact of anthropogenic heat on urban climate in Tokyo, Atmos, Environ. Times 33 (24–25) (1999) 3897–3999, https://doi.org/10.1016/S1352-2310(99)00132-6.

[79] M. Iamarino, S. Beevers, C.S.B. Grimmond, High-resolution (space, time) anthropogenic heat emissions: London 1970–2025, Int. J. Climatol. 32 (11) (2012) 1754–1767, https://doi.org/10.1002/joc.2390.

[80] R. Hamdi, G. Schayes, Sensitivity study of the urban heat island intensity to urban characteristics, Int. J. Climatol. 28 (7) (2008) 973–982, https://doi.org/10.1002/joc.1598.

[81] T.P. Lin, A. Matzarakis, Tourism climate and thermal comfort in sun moon lake, taiwan, Int. J. Biometeorol. 52 (2008) 281–290, https://doi.org/10.1007/s00484-007-0122-7.